Civil Engineering Infrastructures Journal xx,xx

DOI: 10.22059/ceij.2025.384791.2179

SH-Wave Scattering by an Orthotropic Triangular Soft Hill

Mehdi Panji * (Corresponding Author)
Department of Civil Engineering, Za. C., **Islamic Azad University**, Zanjan, Iran.
E-mail: m.panji@iau.ac.ir

Saeed Mojtabazadeh-Hasanlouei
Department of Civil Engineering, Za. C., **Islamic Azad University**, Zanjan, Iran.
E-mail: mojtabazadeh@iauz.ac.ir
Website: www.mojtabazadeh.ir/

Farinaz Saleki
Department of Civil Engineering, Za. C., **Islamic Azad University**, Zanjan, Iran.
E-mail: f.saleki@iauz.ac.ir

Received: 03/11/2024

Revised: 21/01/2025

Accepted: 24/02/2025

Summary

In this paper, the *SH*-wave scattering by an orthotropic triangular soft hill settled on the underlying half-space was investigated using a half-space time-domain boundary element method to obtain a seismic ground response. The surface of the hill and its interface were only discretized by quadratic elements to elaborate on the computational model. First, a brief formulation of the method and the modified boundary integral equation with damping were presented. Then, the method was implemented in a developed DASBEM algorithm and analyzed as a verification example to compare with the literature and confirm the obtained results. Finally, an advanced numerical study was carried out to sensitize the key parameters of the model, including the isotropy factor, shape ratio of the hill, incident wave angle, and frequency content. The results showed that the proposed method had the powerful ability to create sharp corner features. Also,

the orientation of the material texture of the triangular hill was extremely effective on the seismic ground response and changing the amplification patterns.

Keywords: The DASBEM Project, Orthotropic Triangular Hill, Half-Space TD-BEM, *SH*-Wave, Surface Response.

Article Highlights

1. A novel time-domain boundary element method was applied to investigate *SH*-wave scattering by an orthotropic triangular hill on a half-space.
2. The method utilized quadratic elements to model the hill's surface and interface with high accuracy.
3. The DASBEM algorithm implementation verified against existing literature, confirming robustness and result consistency.
4. Parametric analysis revealed that hill shape ratio, incident wave angle, and frequency significantly influence seismic response.
5. Orientation of material texture in the hill notably alters seismic ground amplification patterns.

1. Literature Synopsis

The form of the sites and their constituent materials is important from a geotechnical earthquake engineering point of view to influence the investigation of the propagation of waves and their effects. These factors can affect the waves' intensity, path, and arrival time due to the variety and complexity of constructions. Past research investigated these factors by creating a suitable model for analyzing topographic effects. Two- and three-dimensional analyses were presented by assuming the isotropic or orthotropic behavior of the domain. Reviewing the technical literature and previous research results, the methods used to study different domains and features can be classified into three categories: analytical, semi-analytical, and numerical. In the analytical approaches, by determining the response functions of the governing equations for each unique feature, an accurate answer to the problem is obtained. Some researchers like Gupta *et al.* (2017) studied the reflection of *SH*-waves in an orthotropic layer placed between two different dry sand layers. Selivanov (2019), investigated the presence of cracks and their effects in the orthotropic-domain. The performance of the analytical method for propagating elastic waves in a transversely isotropic poroelastic half-space can be found in Teymouri *et al.* (2021). The second category is semi-analytical approaches, in which the problem is solved by a combination of analytical methods and other methods. In this regard, the T-matrix method or null-field approach (Chen *et al.*, 2012), the region-matching technique (Tsaur *et al.*, 2018) were examples of semi-analytical methods used by researchers. Despite the high accuracy of analytical and semi-analytical methods, they do not have flexibility in modeling complex topographic effects and natural conditions; thus, numerical methods entered the field of calculations due to the progress of computers and their ability to model. The use of numerical scenarios has grown significantly. In the literature, there are various

numerical approaches used to model different topographic features, which can be classified into three categories: volumetric, boundary, and combined methods. The two methods of finite element method (FEM) (Deckers *et al.*, 2018) and finite difference method (FDM) (Hou *et al.*, 2025) are among the most well-known numerical methods. The BEM can be divided into two categories: the full-space and half-space BEM, each of which is developed in two time and frequency-domains. By examining the differences between these two methods, it can be seen that in the full-space BEM, the entire topographic boundary and a large part of the smooth ground surface on the sides of the problem should be meshed, and stress-free boundary conditions should be approximately applied to the surface meshes. The use of the full-space case and its development in the frequency-domain was done by Gao & Lu (2021). In the half-space BEM scenario, due to the automatic satisfaction of the stress-free boundary conditions of the ground surface, only the corrugated boundary of the problem (surface or subsurface) is discretized, and this issue significantly reduces the volume of data and their calculation time compared to the full-space BEM. The researches of Mojtabazadeh *et al.* (2024) can be mentioned, which used the half-space BEM in isotropic and orthotropic media to model the topographic types subjected to *SH*-wave propagation. Moreover, Parvanova *et al.* (2014) used the frequency-domain full-space BEM to investigate the effects of subsurface openings on the seismic response of the surface. The development of numerical methods in orthotropic-domains has received much less attention than the isotropic case. Zheng & Dravinski (1998) studied *SH*-wave propagation in an orthotropic alluvial valley using a frequency-domain BEM approach. Dineva *et al.* (2014) investigated *SH*-wave propagation in an orthotropic half-space with subsurface cavities. Recently, Mojtabazadeh *et al.* (2022a, b) presented the model and algorithm of the damped orthotropic half-space time-domain BEM to obtain the seismic response of the topographic effects of all types of hills, valleys, cavities and inclusions subjected to incident *SH*-wave.

The importance of attention to the hills with different shapes resulting from sedimentation and the accumulation of surface materials over time, and the possibility of placing them in the path of urban projects, including sewage exit routes, subways, urban roads, and streets, etc., indicates the need to know and examine these sediments' behavior, which shows the provision of appropriate standards in the bylaws. On the other hand, the literature showed the lack of a comprehensive presentation of seismic analysis results of orthotropic sharp peak hills. Therefore, in the present work, a heterogeneous triangular hill placed on the orthotropic-domain is considered and analyzed by half-space time-domain BEM subjected to *SH*-wave. To study the mentioned feature, in addition to the development of the method in a general algorithm called The DASBEM Project, previously presented by the authors, and solving the verification example, the results are presented in the framework of a numerical study using the parameters of impedance ratio, input-wave angle, and shape ratio of the hill in the frequency and time-domains. The innovation of the present work can be summarized in developing a step-by-step TD-BEM algorithm to establish the simple model of orthotropic soft sharp-peak hills and obtain some new results to observe the effect of hill material texture on the seismic response of the surface under *SH*-wave propagation.

2. Half-Space TD-BEM Approach

Fig. 1 shows the model of a triangular sedimentary soft hill in an orthotropic half-space domain subjected to incident *SH*-wave. The boundary of the hill and the interface between the hill and the ground are meshed. In this model, Ω represents the domain, which is specified by numbers 1 and 2 for the hill and the underlying domain, respectively. Γ_{ij} is the interface boundary, ρ is the density, μ is the shear modulus, c is the shear wave velocity, and θ is the incident angle of the wavefront. In this model, *SR* is obtained by using the ratio of the height to half-width of the hill, which represents the shape ratio of the hill.

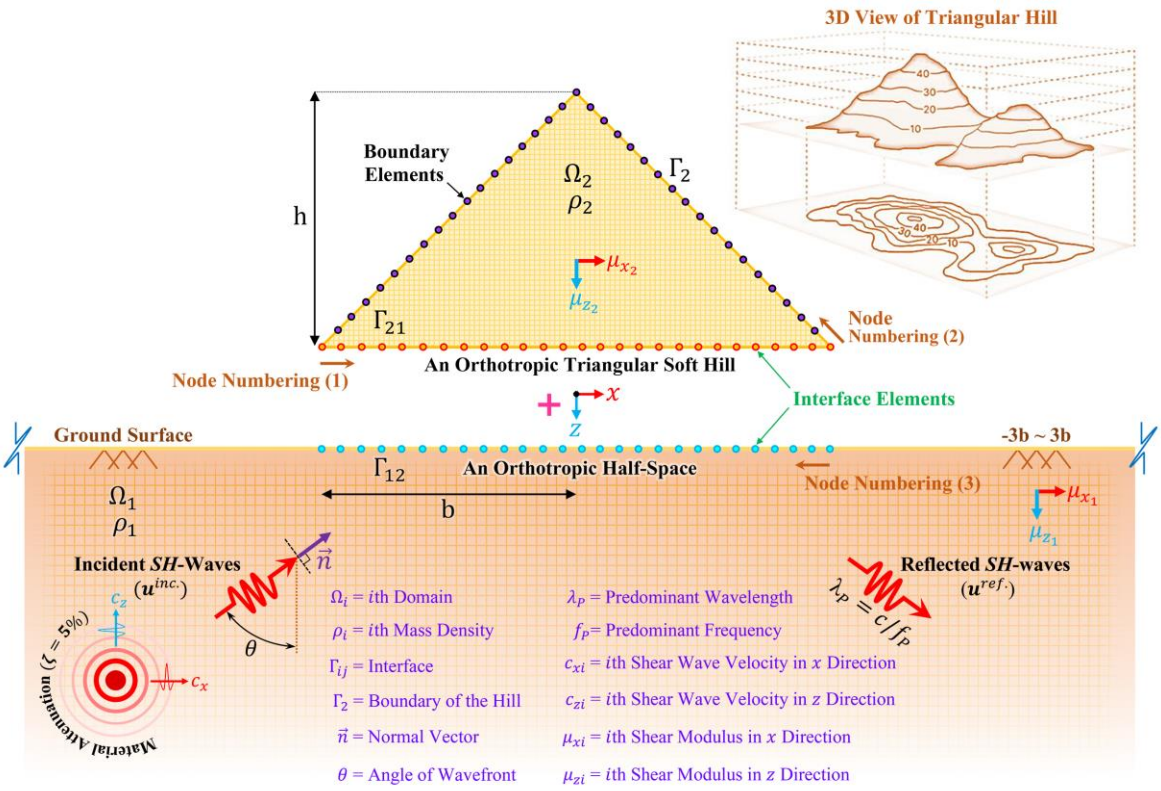

Fig. 1. Geometrical Modeling of the soft triangular soft hill settled on the orthotropic half-space subjected to the propagating incident *SH*-waves.

By assuming an orthotropic half-space domain, the governing wave equation and boundary conditions of the ground surface are as follows:

$$c_{66}\frac{\partial^2 u(x,z,t)}{\partial x^2} + c_{44}\frac{\partial^2 u(x,z,t)}{\partial z^2} + b(x,z,t) = \rho\frac{\partial^2 u(x,z,t)}{\partial t^2}, \quad \textbf{(1)}$$

$$T_y = \left[c_{66}\frac{\partial u}{\partial x}n_x + c_{44}\frac{\partial u}{\partial z}n_z\right]_{z=0} = 0\,, \quad \textbf{(2)}$$

where $u(x,z,t)$ is the out-of-plane displacement at the coordinates (x,z) and at the current time t, c_{66} and c_{44} is the rigidity matrix of an orthotropic medium in two directions, $b(x,z,t)$ is the out-of-plane body force for a point (x,z) and specific time t, ρ is the density of material, T_y is the shearing stress on the surface and *n* is the normal vector perpendicular to the ground surface where presented by n_x and n_z on x and z axes (Mojtabazadeh *et al.*, 2022a). In this model, the input seismic wave is of the Ricker function type. The equation of this wave is according to the following equation:

$$f(t) = \left[1 - 2\left(\pi\, f_p (t - t_0)\right)^2\right] e^{-\left(\pi\, f_p (t-t_0)\right)^2}, \tag{3}$$

where f_p is the predominant frequency of the wave, t_0 is the time-shift parameter. By satisfying the stress-free boundary conditions and modeling the medium as a half-space, the displacement of the free-field (u^{ff}) is obtained by considering the incoming and reflected waves as follows:

$$u^{ff}(x,z,t) = a_{max} \cdot \left(\begin{array}{l} \left[1 - 2\left(\dfrac{\pi\, f_p}{c}\, \alpha^{inc.}\right)^2\right] e^{-\left(\frac{\pi\, f_p}{c}\alpha^{inc.}\right)^2} H\left(t - \dfrac{r^{inc.}}{c}\right) + \\ \left[1 - 2\left(\dfrac{\pi\, f_p}{c}\, \alpha^{ref.}\right)^2\right] e^{-\left(\frac{\pi\, f_p}{c}\alpha^{ref.}\right)^2} H\left(t - \dfrac{r^{ref.}}{c}\right) \end{array} \right), \tag{4}$$

where a_{max} is the maximum amplitude of the input motion, $\alpha^{inc.}$ and $\alpha^{ref.}$ are the phases of the incoming and reflected waves in the distances are $r^{inc.}$ and $r^{ref.}$, respectively. Now, by simultaneously solving equations (1) and (2), the half-space fundamental solutions used in the Boundary Integral Equation (BIE) will be obtained. The BIE in the time-domain is defined in the following section.

2.1 The Damped BIE

The material damping is a significant parameter in wave propagation to obtain the displacement field of the orthotropic problem. The Barkan method is used in the present TD-BEM approach. Based on the mentioned approach, a constant reduction in the response range is applied to converge the response at the large time steps. By applying material damping in the time-domain, the BIE is obtained as follows:

$$c(\boldsymbol{\xi})u(\boldsymbol{\xi},t) = \int_\Gamma \left\{ \int_0^t \left[\begin{array}{l} u^*(\boldsymbol{x},t;\boldsymbol{\xi},\tau)\cdot q(\boldsymbol{x},\tau)\cdot e^{-2\pi\zeta(t-\tau)} - \\ q^*(\boldsymbol{x},t;\boldsymbol{\xi},\tau)\cdot u(\boldsymbol{x},\tau)\cdot e^{-2\pi\zeta(t-\tau)} \end{array} \right] d\tau \right\} d\Gamma(\boldsymbol{x}) + u^{ff}(\boldsymbol{\xi},t)\,, \tag{5}$$

In this regard, Γ represents the boundary of the problem, $c(\xi)$ is the refractive index of the geometry, u^{ff} is the free-field displacement, and ζ represents the damping of the half-space domain. u^* and q^* are the transient orthotropic Green's functions for the displacement and traction fields, respectively. Also, $\boldsymbol{\xi}$ is the location of the wave propagation source, and $\boldsymbol{x}$ is the point of

receiving the wave. The integrals in the mentioned formula are $u^* \cdot q$ and $q^* \cdot u$ Riemann convolution integrals (Mojtabazadeh *et al.*, 2022b). The time integrals are calculated by discretizing the time axis into N parts equal to the interval Δt using the linear temporal shape functions. To calculate the spatial integrals, the corrugated boundary of the feature and the interface is meshed by three-node quadratic elements. Therefore, the integral form of BIE (Eq. 5) can be displayed in the following total-limit form:

$$c(\boldsymbol{\xi})u^N(\boldsymbol{\xi}) = \sum_{n=1}^{N}\sum_{m=1}^{M}\left[\begin{array}{l}\left\{\int_{\Gamma_m}[U_1^{N-n+1}(\boldsymbol{x}(\kappa),\boldsymbol{\xi}) + U_2^{N-n}(\boldsymbol{x}(\kappa),\boldsymbol{\xi})]N_\alpha(\kappa)|J|\,d\kappa\right\}q_\alpha^n - \\ \left\{\int_{\Gamma_m}[Q_1^{N-n+1}(\boldsymbol{x}(\kappa),\boldsymbol{\xi}) + Q_2^{N-n}(\boldsymbol{x}(\kappa),\boldsymbol{\xi})]N_\alpha(\kappa)|J|\,d\kappa\right\}u_\alpha^n\end{array}\right] + u^{ff.N}(\boldsymbol{\xi}), \quad \textbf{(6)}$$

where N represents the number of time steps, M is the number of elements, and Γ_m is the boundary on which m elements are located. Also, N_α represents the shape functions, which are $\alpha = 1, 2, 3$; κ shows the local coordinates of the elements in the use of the Jacobian determinant, $|J|$, to convert Cartesian coordinates. In this regard, U_1^{N-n+1} & U_2^{N-n} and Q_1^{N-n+1} & Q_2^{N-n} are the condensed form of the half-space orthotropic scalar kernels for the displacement and traction fields, respectively. Moreover, the value of free-field displacements in time step N is shown by $u^{ff.N}$.

2.2 Deployment

To solve the above discretized BIE, a ten-point Gaussian numerical integration for all non-singular boundary elements is used to obtain the step-by-step equation as follows:

$$\sum_{n=1}^{N}\boldsymbol{H}^{N-n+1}\{\boldsymbol{u}^n\} = \sum_{n=1}^{N}\boldsymbol{G}^{N-n+1}\{\boldsymbol{q}^n\} + \{\boldsymbol{u}^{ff.N}\}, \quad \textbf{(7)}$$

where the coefficient matrices $\boldsymbol{H}^{N-n+1}$ and $\boldsymbol{G}^{N-n+1}$ are obtained by integrating over the boundary elements of the orthotropic-domain for the displacement and traction fields and the vectors of $\{\boldsymbol{u}^n\}$ and $\{\boldsymbol{q}^n\}$ are the boundary displacement and traction fields, respectively. To convert this equation into a solvable form, the following form can be obtained after applying the boundary conditions:

$$[\boldsymbol{A}_1^1]\{\boldsymbol{X}^N\} = [\boldsymbol{B}_1^1]\{\boldsymbol{Y}^N\} + \{\boldsymbol{R}^N\} + \{\boldsymbol{u}^{ff.N}\}, \quad \textbf{(8)}$$

In this equation, the coefficient matrices $[\boldsymbol{A}_1^1]$ and $[\boldsymbol{B}_1^1]$ are the matrices corresponding to unknown and known boundary values, respectively, and the vectors $\{\boldsymbol{X}^N\}$ and $\{\boldsymbol{Y}^N\}$ are the values of unknowns and known boundary, respectively, and the vector $\{\boldsymbol{R}^N\}$ is the effect of dynamic history in the current node N as follows:

$$\{\boldsymbol{R}^N\} = \sum_{n=1}^{N-1}(\boldsymbol{G}^{N-n+1}\{\boldsymbol{q}^n\} - \boldsymbol{H}^{N-n+1}\{\boldsymbol{u}^n\}), \quad \textbf{(9)}$$

2.3 Convex Inhomogeneity

To develop a heterogeneous orthotropic model with half-space BEM, it is essential to employ the sub-structuring method and ensure continuity conditions are met at the interface. By executing the analysis at each time-step using assembled matrices, Eq. (7) transforms into Eq. (10):

$$H_{12}^{1}\, u_{12}^{N} = G_{12}^{1}\, q_{12}^{N} + R_{12}^{N} + u_{12}^{ff.N}, \tag{10}$$

Here, u_{12}^{N} and q_{12}^{N} represent the variables on the interface Γ_{12}, while $u_{12}^{ff.N}$ denotes the free-field motion at the interface. Additionally, R_{12}^{N} reflects the interface's previous dynamic time-history at time-step *N*, as shown in Eq. (11):

$$R_{12}^{N} = \sum_{n=1}^{N-1} (G_{12}^{N-n+1}\, q_{12}^{n} - H_{12}^{N-n+1}\, u_{12}^{n}), \tag{11}$$

Similarly, the equations for the sedimentary hill, Eqs. (10) and (11), will now become Eqs. (12) and (13):

$$H_{21}^{1}\, u_{21}^{N} = G_{21}^{1}\, q_{21}^{N} + R_{21}^{N}, \tag{12}$$

and,

$$R_{21}^{N} = \sum_{n=1}^{N-1} (G_{21}^{N-n+1}\, q_{21}^{n} - H_{21}^{N-n+1}\, u_{21}^{n}), \tag{13}$$

As shown in Fig. (1), symbol (12) corresponds to the half-space interface associated with the hill (Γ_{21}), while (21) denotes the hill interface connected to the half-space. Likewise, u_{21}^{N} and q_{21}^{N} represent the respective fields associated with interface Γ_{21}.

2.4 Integrated Equation

Through coupling Eqs. (10) to (13), the unknown interface variables are determined, leading to the resolution of the problem. Consequently, the interface continuity conditions for compatibility can be expressed as Eqs. (14) and (15):

$$u_{12}^{N} = u_{21}^{N}, \tag{14}$$

and,

$$\mu^{(1)} \cdot q_{12}^{N} = -\mu^{(2)} \cdot q_{21}^{N} , \tag{15}$$

The equivalent rigidity moduli for the half-space and the hill are denoted by $\mu^{(1)}$ and $\mu^{(2)}$, respectively. Additionally, q_{12}^{N} and q_{21}^{N} represent the traction paths along the hill's interface. The equivalent rigidity modulus at each interface node is provided in Eq. (16):

$$\mu^{(j)} = c_{66} \cdot n_x + c_{44} \cdot n_z , \tag{16}$$

The equivalent rigidity modulus for the jth medium is denoted by $\mu^{(j)}$, with shear moduli μ_x and μ_z represented by c_{66} and c_{44}, respectively, while n_x and n_z are the components of the normal vector. The final matrix form of the coupled orthotropic equations at each time-step is provided in Eq. (17), which identifies all the unknown interface variables.

$$\begin{bmatrix} H_{12}^{1} & H_{1}^{1} & 0 & \dfrac{-1}{\mu^{(1)}} G_{12}^{1} \\ H_{21}^{1} & 0 & H_{2}^{1} & \dfrac{1}{\mu^{(2)}} G_{21}^{1} \end{bmatrix} \begin{Bmatrix} u_{12}^{N} \\ u_{1}^{N} \\ u_{2}^{N} \\ q_{12}^{N} \end{Bmatrix} = \begin{Bmatrix} R_{12}^{N} \\ R_{21}^{N} \end{Bmatrix} + \begin{Bmatrix} u_{12}^{ff.N} \\ 0 \end{Bmatrix}, \tag{17}$$

2.5 The DASBEM Project

A DASBEM algorithm was developed for the dynamic analysis of *SH*-wave scattering problems based on the orthotropic half-space TD-BEM using MATLAB programming language to investigate sharp peak hills with different geometric characteristics. First, the program receives the geometric attributes of the problem, the material type, and the input-wave information as input data to analyze the problem and obtain all the boundary unknowns. The results of this analysis are shown in 2D/3D graphical form at the end of the post-processing part of the program. In the present work, the orthotropic triangular hill, the underlying orthotropic half-space, and the *SH* seismic wave are the inputs of the algorithm. The details of The DASBEM Project can be found in Mojtabazadeh *et al.* (2022a) and www.dasbem.ir.

3. Framework

According to the method used in the present work, the orthotropic half-space TD-BEM approach, the triangular hill settled on the ground is separated from the tangent boundary (interface). As can be seen in Fig. 1, the first domain is an open orthotropic half-space subjected to incident anti-plane *SH*-waves, and the second domain is a completely discretized closed triangular hill. All nodes of the first domain are indicated by the subscript (12) so that the G.S. shows the surface of the ground,

and the dimensionless factor x/b is the ratio of the surface to the half-width of the hill. The ratio of the horizontal to vertical shear wave velocity field is indicated by the symbol IF, which is obtained from the relation $IF = \sqrt{\mu_x/\mu_z}$ in an orthotropic medium with a constant density, and that is called the Isotropy Factor henceforth (Zheng and Dravinski, 1998). μ_x and μ_z are respectively the shear modules of the domain in the x and z directions, which is called an isotropic case if the two values are equal. But, according to the purpose of the research, which is to investigate the orthotropic pattern of the domain, in addition to $\mu_x = \mu_z$, two states, $2\mu_x = \mu_z$ and $\mu_x = 2\mu_z$, are also investigated to create isotropy factors of 0.707 and 1.414, respectively. The second domain is a triangular closed medium, where all the nodes belonging to its interface are represented by the subscript (21). In this topography, SR represents the shape ratio of the hill settled on the ground obtained from the ratio h/b, so that h is the height of the triangular hill and b is the half-width of the feature. η represents the dimensionless frequency calculated as $\eta = \omega b/\pi c$, in which ω is the angular frequency of the wave, b is the half-width of the topography, and c is the equivalent shear wave velocity of the domain. To achieve fast convergence of the response and obtain stable results, 5% material damping (ζ) is considered, and as mentioned earlier, Ricker's wave type is used for obliquely incoming out-of-plane *SH* waves by incidence angle of (θ). Considering that the orthotropic case for the soil (half-space) and sedimentary rocks (hill) have different characteristics, therefore, in this model, the properties of sandstone and shale (Schön, 2015) are considered. Thus, the average shear-wave velocity (c_1) and density (ρ_1) of the half-space are specified as 1150 m.s^{-1} and 2400 kg.m^{-3}, respectively, while the corresponding values for the feature are 900 m.s^{-1} and 2300 kg.m^{-3} as c_2 and ρ_2. Based on this, the impedance ratio ($I = \rho_2 c_2/\rho_1 c_1$) of the feature to the half-space is equal to 0.75, indicating that the materials forming the hill are 25% softer compared to the underlying space.

3.1 Verification

To verify the results of the seismic analysis of the soft triangular hill settled on the orthotropic half-space under *SH*-waves, the results of Lin *et al.* (2010) are used to obtain the surface response in the range of -2.5b to 2.5b. In this model, the shear wave velocity (c) is equal to 800 m.s^{-1}, and the density in the isotropic state is equal to 1.0 ton.m^{-3}. To model the triangular hill, 150 and 55 boundary elements are considered on the hill and the interface with the underlying half-space. This problem is solved with 500 time-steps for a total time of 6 seconds. The dimensionless frequency (η) of the validation results is equal to 0.50, and the wave incident angle is vertically propagated (θ=0). To check the agreement of the response with the results of Lin *et al.* (2010), the isotropic factor (IF) of 1.414 is used to indicate the orthotropic state of the problem. The solution to the problem is continued by reducing this factor until reaching the isotropic state (IF=1.0) in 6 different modes of responses. As can be seen in Fig. 2, by reducing the IF, the results are closer to the response of Lin *et al.* (2010) and finally, they have coincided in the isotropic state.

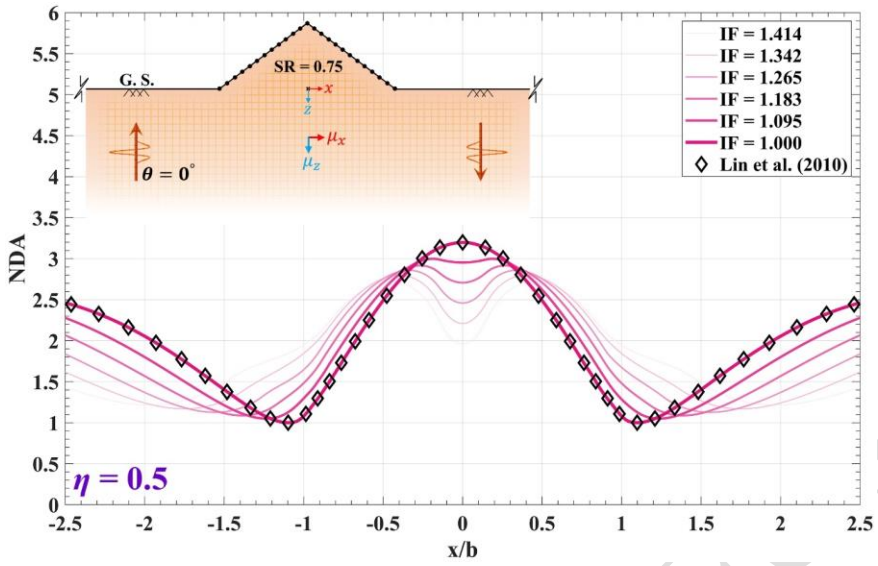

Fig. 2. Validation of the results for an orthotropic triangular soft hill settled on the orthotropic half-space subjected to vertically propagating incident anti-plane *SH*-waves with different isotropy factors.

3.2. Snapshot Imagery

The snapshot imagery is used to observe the distribution of *SH* seismic waves in an orthotropic triangular soft hill and underlying half-space. In these images (Figs. 3 and 4), the wave propagation is shown in different values of IF at specific times. These images were obtained at IF values equal to 1.414, and 0.707 in the range of -3b to 3b at times of 0.5, 1.0, 1.5, and 2.0 seconds. The same times are chosen for all IFs so that the comparison of wave reflection results can be correctly done. To prepare these images, 12880 numbers of internal points are used as display pixels. These points are treated as observation points within the domain, where the seismic response is calculated. The numerical method employed in this research is based on the Boundary Element Method (BEM). Since BEM inherently reduces the dimensionality of the problem (modeling only the boundary rather than the entire domain), the response at internal points is not directly calculated during the main solution process. Instead, after solving for the boundary variables (e.g., displacement or traction), the response at internal points is computed using the boundary integral equations. This process involves evaluating the Green's functions for the half-plane and integrating their contributions from the boundary elements to the internal points. Specifically, for each internal point, the response is obtained by summing up the influence of all boundary elements based on their solved boundary values. By observing and comparing the images, the hill effect on wave propagation is well shown. As can be seen in figures, at a time of 0.5 sec. and IF of 1.414, the dispersion of waves occurred mostly inside the triangular hill and on the surface close to the ground. Since the IF is greater than unity (IF>1.0), the value of μ_x is greater than μ_z, and the reflected waves spread more along the horizon. By reducing the IF, the ring wave propagation deepens, and their penetration into the underlying layers increases at the same time. In other words, the reflected waves spread more in the vertical direction by increasing the value of μ_z and

decreasing μ_x. On the other hand, at a constant IF, the wave distribution in depth increases as time passes, and the halo radius of the reflected waves becomes larger. However, at 2 seconds, the waves reflected from the hill and the half-space boundaries are assembled to strengthen the interference of the reflected waves.

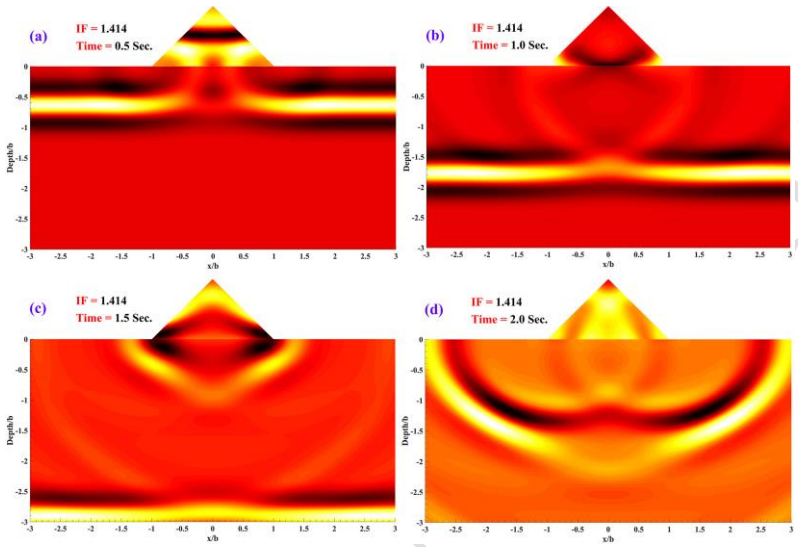

Fig. 3. Snapshot imagery chosen at the four times for an orthotropic triangular soft hill settled on the orthotropic half-space subjected to vertically incident *SH*-waves with IF equal to 1.414.

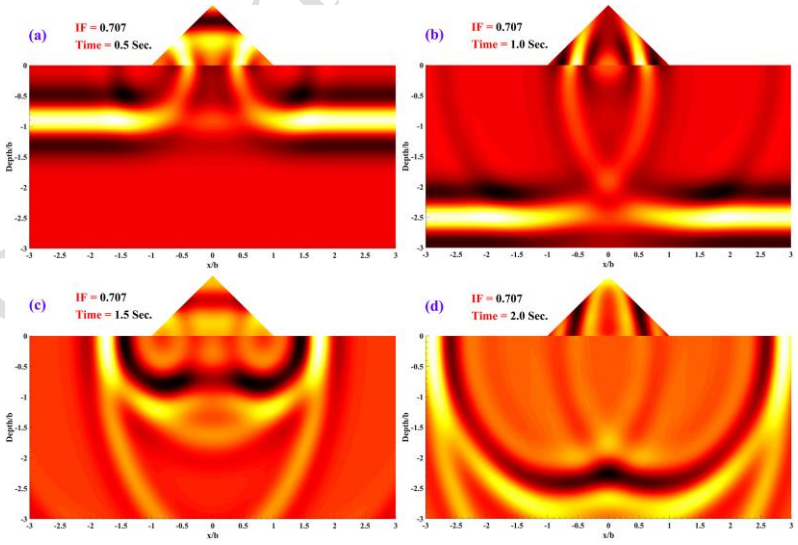

Fig. 4. Snapshot imagery chosen at the four times for an orthotropic triangular soft hill settled on the orthotropic half-space subjected to vertically incident *SH*-waves with IF equal to 0.707.

3.3 Temporal Results

In Figs. (5) and (6), the response of the hill surface and its surroundings can be seen in the time-domain subjected to obliquely incident *SH*-waves. In all cases, the shape ratio of the model is considered equal to 1.0 to keep the dimensions constant, and the results are presented in the range of -3b to 3b from the surface. Two incident angles are considered, including 0, and 90 degrees. As mentioned above, the IF is a ratio of the vertical and horizontal shear modulus of the domain materials. Therefore, three different cases, including 1.414, 1.0, and 0.707, are considered for IFs to show the effect of ground patterns in time history responses. As can be seen in Fig. (5), when the seismic waves propagate vertically, the scattering and diffraction of the wave on the surface happen completely in parallel, but the duration of the dispersion of the reflected waves is different over time and depends on the IF. The maximum propagation time of the reflected waves can be seen in the IF equal to 1.414, in which the horizontal shear modulus is greater than the vertical one, and the propagated wave in the orthotropic-domain is reflected intermittently. The propagation time of the reflected waves is reduced by decreasing the IF. Fig. (6) shows the synthetic seismogram of the surface for horizontally incident *SH*-waves. According to the waves reaching the surface and their reflection, it is observed that the state of symmetry is not established and the time of arrival of the incident wave to different parts of the ground and hill surfaces is different. Like the vertical propagation of waves, the longest temporal reflection occurs in the IF of 1.414, and the duration of the wave reflection is also reduced by decreasing this factor. Therefore, in the IF of 0.707, the dispersion time of the reflected waves is shorter and the incoming wave exits the domain easily and quickly, considering that the vertical shear modulus is greater than its horizontal value.

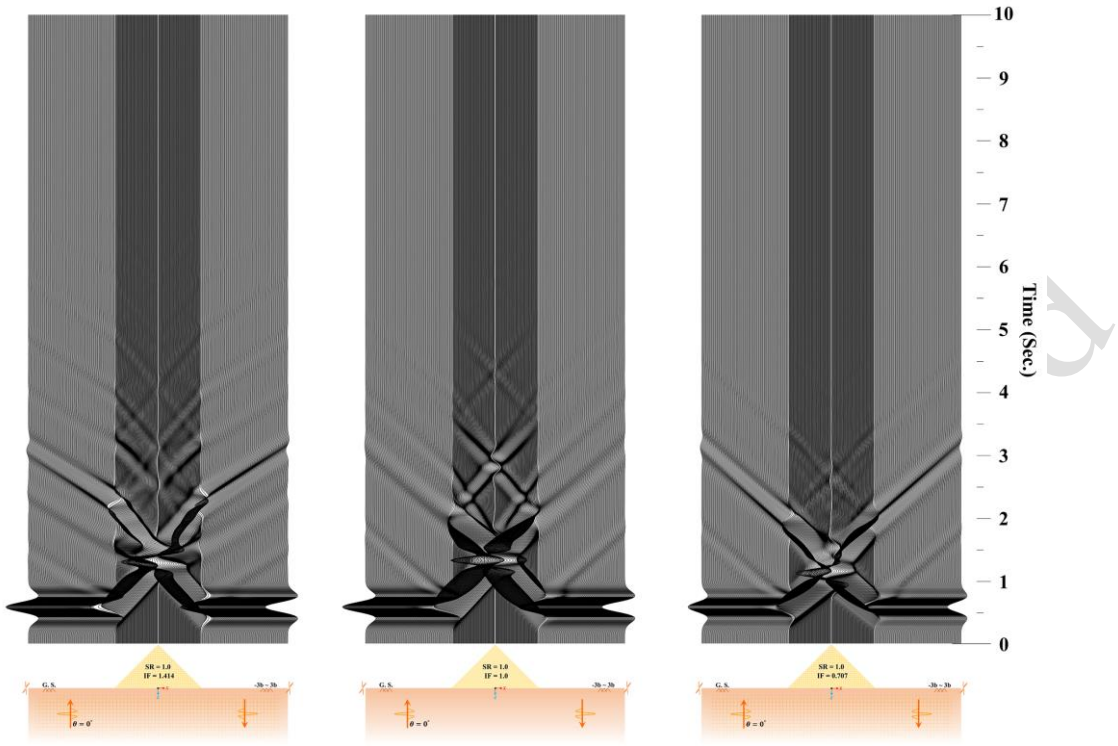

Fig. 5. Synthetic seismogram of the surface in the presence of an orthotropic triangular soft hill (SR=1.0) subjected to vertically incident *SH*-waves in three different *IF*s.

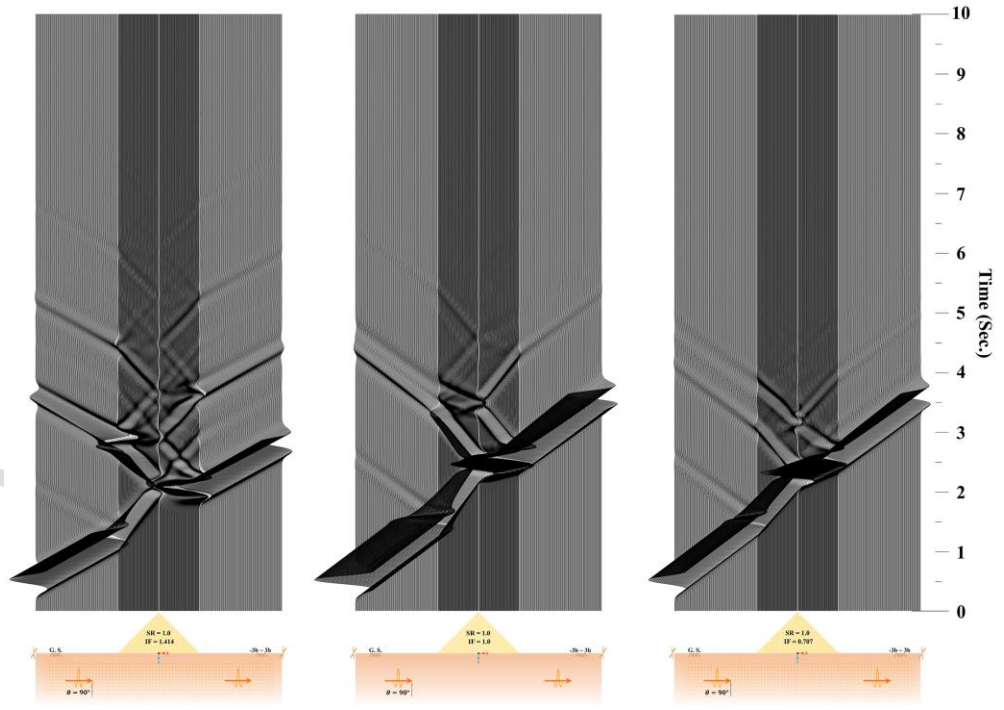

Fig. 6. Synthetic seismogram of the surface in the presence of an orthotropic triangular soft hill (SR=1.0) subjected to *SH*-waves with incident angle of 90^{o} in three different *IF*s.

3.4 Surface Normalized Displacement

Figs. (7) and (8) are presented to compare the situation of the incident seismic waves on the triangular hill surface and beyond in the frequency-domain. The normal displacement amplitude (NDA) is obtained on the surface in terms of the hill shape ratio (SR) which represents the ratio between the Fourier amplitude of motion at the surface and that of the incident motion which is the ratio of the Fourier amplitude of surface motion to the Fourier amplitude of incident motion, the dimensionless frequency (η), the wave incident angle (θ), and different IFs. As can be seen in figures, the NDA is presented at SR=1.0 at four dimensionless frequencies (η), including 1.0, and 2.0 for three different IFs based on three cases of the ground deposit texture. As shown in figures, higher frequencies have intensified the fluctuations but, the NDA on the hill surface and the smooth ground surface of the sides decreases with increasing incident wave angle relative to the vertical direction. In the orthotropic case with IF=1.414, where the horizontal shear modulus is twice the vertical one, waves propagate more horizontally, resulting in less displacement, with a maximum value of 2.79 for $\theta = 0°$ and $\eta = 1.0$ (Fig. 7a). This reduction occurs compared to the other two IFs due to the weaker interaction of waves with the triangular hill slopes. However, the results are different for IF equal to 1.0 and 0.707. In the case of IF=0.707, the arrival of oblique seismic waves causes the greatest displacement at the top of the hill with the maximum value of 5.28 for $\theta = 30°$ and $\eta = 2.0$ (Fig. 8b) compared to the isotropic case (IF=1.0). The NDA for the factor of 1.414 has the same conditions across all dimensionless frequencies.

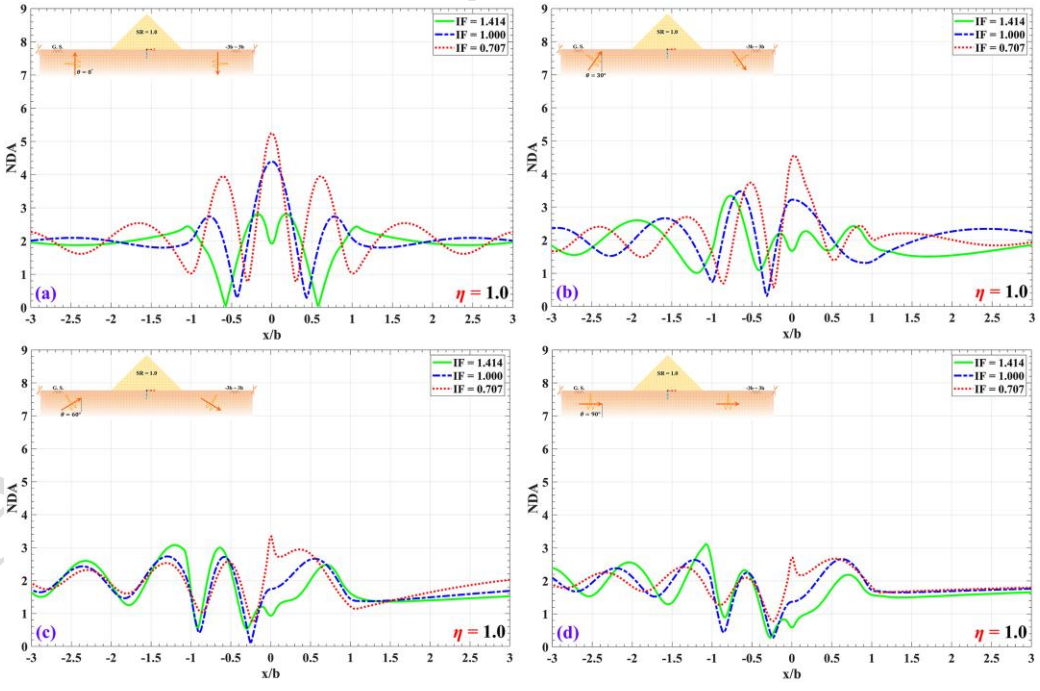

Fig. 7. The normalized displacement amplitude of the orthotropic triangular soft hill surface and its beyond (SR=1.0) at the dimensionless frequency of 1.0 in three cases of IF subjected to oblique incident *SH*-wave with angle of 0°, 30°, 60° and 90°.

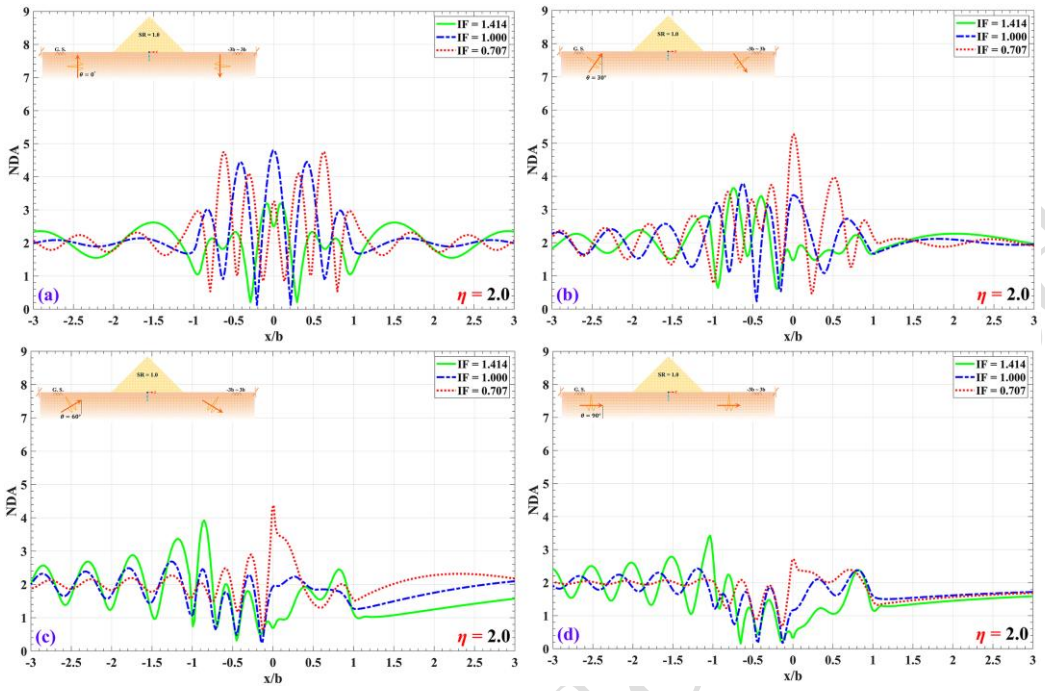

Fig. 8. The normalized displacement amplitude of the orthotropic triangular soft hill surface and its beyond (SR=1.0) at the dimensionless frequency of 2.0 in three cases of *IF* subjected to oblique incident *SH*-wave with angle of 0º, 30º, 60º and 90º.

3.5 Frequency-Domain Amplification Patterns

Presenting the results within the frequency domain offers an unparalleled approach to reveal the overall trend of ground surface displacements around a convex heterogeneous feature and to demonstrate its behavior under seismic wave impact. Therefore, Figs. (9) and (10) show the 3D amplification patterns of the orthotropic triangular soft hill surface and its surrounding area subjected to propagating obliquely incident anti-plane *SH*-waves. The range of the surface is considered between -3*b* and 3*b* around the topography. The results are presented for SR equal to 1.0 at dimensionless frequencies between the values of 0.25 and 5.0. Other variables are similar to the previous time-domain results. For a vertical wavefront (Fig. 9), an isotropy factor (*IF*) of 0.707 produced the highest amplification of 3.71 at the hill's apex, while the amplification pathways were concentrated along the hillside at a slightly lower value of 2.68. A comparison of these patterns reveals that, with *IF*=0.707, distinct maximum points emerged, whereas at *IF*=1.414, amplification appeared in continuous lines. For a horizontal wavefront (Fig. 10), maximum amplification reaches 2.4 at *IF*=0.707. Additionally, at *IF*=1.414, resistance to wave entry into the hill is increased, reducing the maximum amplification to 1.86.

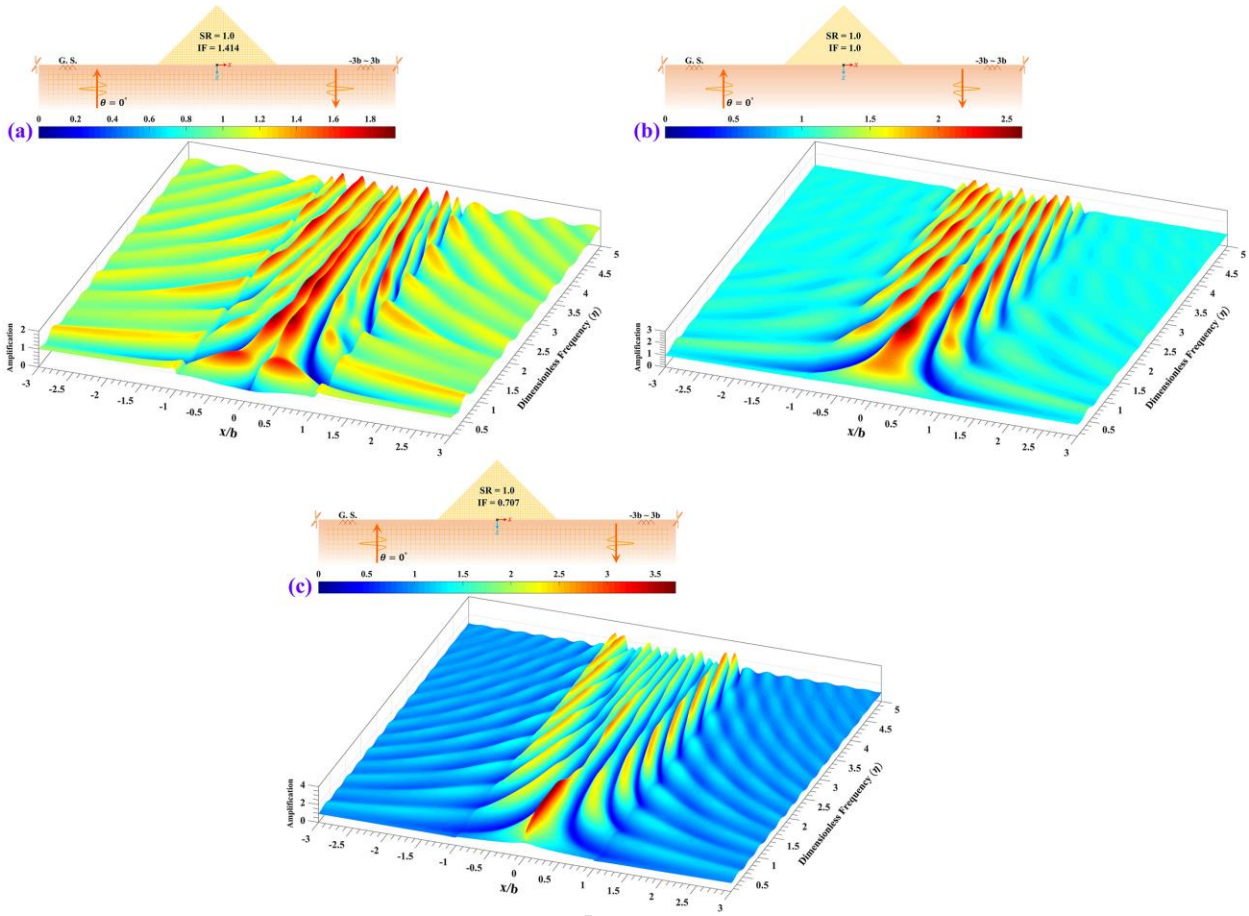

Fig. 9. The 3D amplification ratio of the orthotropic triangular soft hill surface and its surrounding (SR=1.0) subjected to vertically propagating incident anti-plane *SH*-wave in the three different *IF*s.

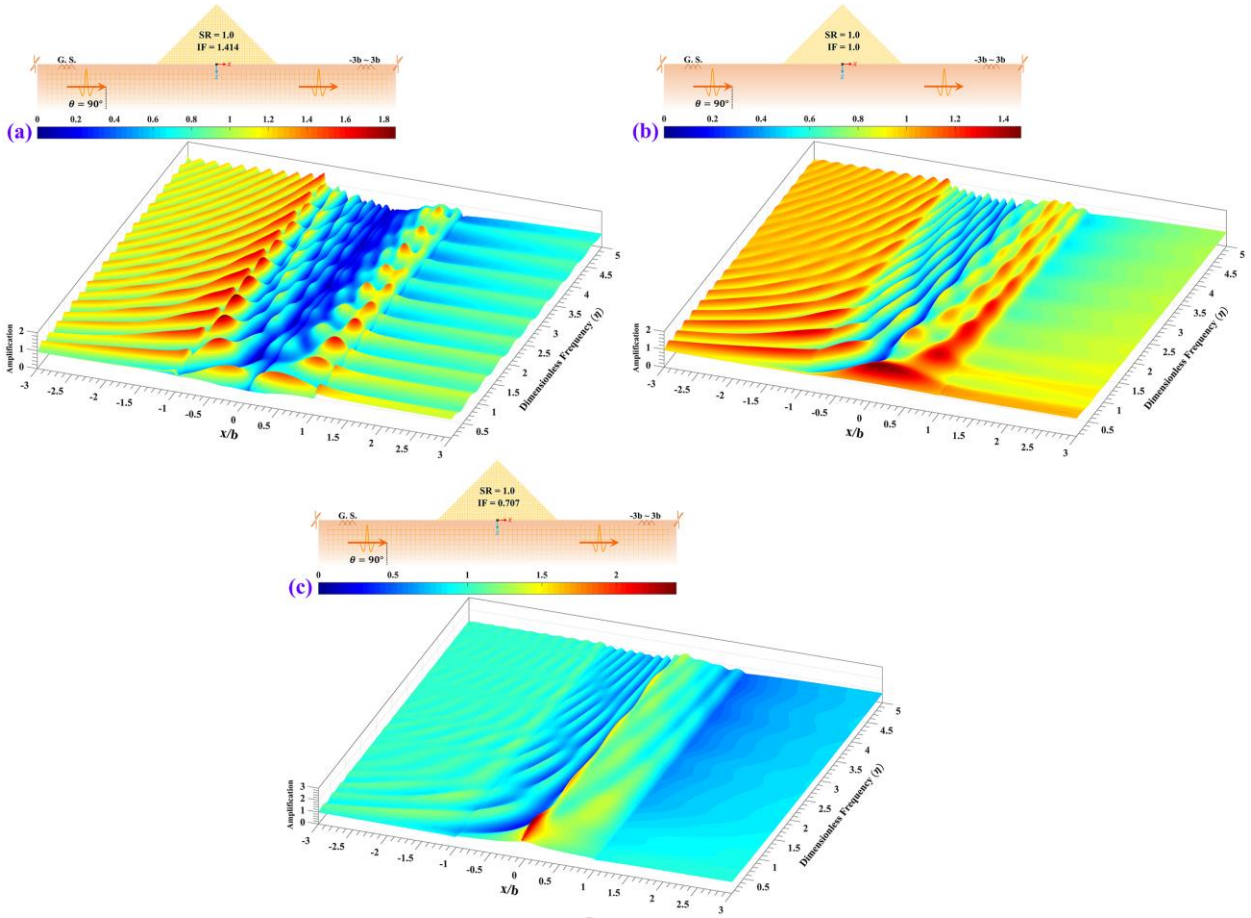

Fig. 10. The 3D amplification ratio of the orthotropic triangular soft hill surface and its surrounding (SR=1.0) subjected to horizontally propagating incident anti-plane *SH*-wave in the three different *IF*s.

4 Conclusions

The *SH*-wave scattering in the presence of an orthotropic triangular soft hill settled on the orthotropic underlying half-space was investigated by a numerical half-space TD-BEM approach to obtain the surface seismic response. The interface between the hill and the underlying half-space and the hill's convex surface needed to be discretized. After implementing the approach in the developed DASBEM algorithm and solving a verification example, it was seen that the method had a powerful ability to create the model of sharp corner features. Then, the seismic surface response was obtained in the time and frequency-domains by considering some model key parameters, including the isotropy factor (IF), the shape ratio of the hill (SR), the incident wave angle (θ), and the frequency content. The most important results of the parametric study can be summarized as follows:

1. **Effect of Isotropic Factor (IF) on Wave Propagation:** The IF ratio was one of the effective factors in determining the direction and depth of the reflected waves so that in IF>1.0, the scattered waves moved more along the horizon to expand the majority of the

propagated waves in this direction; and in contrast, in IF<1.0, the scattered waves were mostly directed in the vertical path to create a vertical wave flow. This indicates that the material properties of the hill significantly affect wave penetration and amplification limits across varying conditions, highlighting the complexity of seismic wave interactions with the hill's geometry.

2. **Effect of Isotropic Factor (IF) on Amplification:** For a vertical wavefront with an IF of 0.707, the highest amplification value of 3.71 is observed at the hill's apex. Conversely, increasing the IF to 1.414 shifts the amplification pattern to continuous lines, concentrating the maximum amplification at the foothill, suggesting that the material properties of the hill limit wave penetration.
3. **Influence of Wave Angle on Amplification Distribution:** When the wavefront is angled at 90°, the amplification focuses for IF=1.414 moves toward the hill's slope, achieving a maximum of 1.82. This suggests that a higher isotropy factor drives incident waves toward the slope, resulting in lower amplification.

Despite certain limitations inherent in boundary element methods (BEM) including complex formulations and slower advancements in handling plastic, nonlinear, and multiphase media, the authors strive to transcend these challenges. By integrating the current method with other approaches, they aim to unlock new potential for nonlinear analysis of intricate topographic features.

ORCID Profiles

Mehdi Panji*: http://orcid.org/0000-0002-3240-7775

Saeed Mojtabazadeh-Hasanlouei: http://orcid.org/0000-0001-8508-4837

The Role of The Authors

1. Mehdi Panji, serving as both the supervisor and founder of The DASBEM Project, played a significant role in shaping the initial concept and proposal for this innovative program. This program is specifically designed to address the complexities and unique characteristics of orthotropic models, enabling more accurate and efficient analyses in various applications. His insights and expertise have been crucial in steering the project towards its objectives.

2. Saeed Mojtabazadeh-Hasanlouei, serving as a post-doctoral fellow in geotechnical engineering, has played a role in both the formulation and implementation of the advanced algorithm known as The DASBEM Project. In addition to his contributions to the algorithm's development, he has also overseen the preparation of figures and the graphical processing of the resulting data. For more information, visit his website: www.mojtabazadeh.ir.

3. Farinaz Saleki, currently a Ph.D. candidate in Geotechnical Engineering, has taken on the responsibility of writing and compiling the manuscript. Her role encompasses not only the development of content but also the organization and integration of research findings, ensuring that the manuscript meets the standards of academic rigor and clarity required for publication.

Data Availability

The data underlying this paper will be shared on reasonable request with the corresponding author (Mehdi Panji).

The authors will provide the journal with any required information, including computational codes, prepared programs, high-quality figures, etc.

Figure Captions:

Fig. 1. Geometrical Modeling of the soft triangular soft hill settled on the orthotropic half-space subjected to the propagating incident *SH*-waves.

Fig. 2. Validation of the results for an orthotropic triangular soft hill settled on the orthotropic half-space subjected to vertically propagating incident anti-plane *SH*-waves with different isotropy factors.

Fig. 3. Snapshot imagery chosen at the four times for an orthotropic triangular soft hill settled on the orthotropic half-space subjected to vertically incident *SH*-waves with *IF* equal to 1.414.

Fig. 4. Snapshot imagery chosen at the four times for an orthotropic triangular soft hill settled on the orthotropic half-space subjected to vertically incident *SH*-waves with *IF* equal to 0.707.

Fig. 5. Synthetic seismogram of the surface in the presence of an orthotropic triangular soft hill (SR=1.0) subjected to vertically incident *SH*-waves in three different *IF*s.

Fig. 6. Synthetic seismogram of the surface in the presence of an orthotropic triangular soft hill (SR=1.0) subjected to *SH*-waves with incident angle of 90^o in three different *IF*s.

Fig. 7. The normalized displacement amplitude of the orthotropic triangular soft hill surface and its beyond (SR=1.0) at the dimensionless frequency of 1.0 in three cases of *IF* subjected to oblique incident *SH*-wave with angle of 0^o, 30^o, 60^o and 90^o.

Fig. 8. The normalized displacement amplitude of the orthotropic triangular soft hill surface and its beyond (SR=1.0) at the dimensionless frequency of 2.0 in three cases of *IF* subjected to oblique incident *SH*-wave with angle of 0^o, 30^o, 60^o and 90^o.

Fig. 9. The 3D amplification ratio of the orthotropic triangular soft hill surface and its surrounding (SR=1.0) subjected to vertically propagating incident anti-plane *SH*-wave in the three different *IF*s.

Fig. 10. The 3D amplification ratio of the orthotropic triangular soft hill surface and its surrounding (SR=1.0) subjected to horizontally propagating incident anti-plane *SH*-wave in the three different *IF*s.

References:

Gao, Y., & Lu, W. (2021). Wave scattering in layered orthotropic media I: A stable PML and a high-accuracy boundary integral equation method. *arXiv*. 10.48550/arXiv.2111.08989.

Chen, J. T., Lee, J., & Shyu, W. (2012). *SH*-wave scattering by a semi-elliptical hill using a null-field boundary integral equation method and a hybrid method. *Geophysical Journal International*, 188, 177-194. 10.1111/j.1365-246X.2011.05240.x.

Dineva, P., Manolis, G., Rangelov, T., & Wuttke, F. (2014). *SH*-wave scattering in the orthotropic half-plane weakened by cavities using BIEM. *Acta Acustica united with Acustica*, 100, 266-276. 10.3813/AAA.918706.

Deckers, E., Jonckheere, S., Van Belle, L., Claeys, C., Desmet, W., (2018). Prediction of transmission, reflection and absorption coefficients of periodic structures using a hybrid Wave Based-Finite Element unit cell method, *Journal of Computational Physics*, 356, 282-302. 10.1016/j.jcp.2017.12.001.

Gupta, S., Smita, S., & Pramanik, S. (2017). Reflection and refraction of *SH*-waves in an orthotropic layer sandwiched between two distinct dry sandy half-space. *Procedia Engineering*, 173, 1146-1153. 10.1016/j.proeng.2016.12.084.

Hou, S., Li, J., Sun, L., (2025). A GFDM with radial PML for SH-wave scattering problems in an orthotropic half plane, *Applied Mathematics Letters*, 171, 109661. 10.1016/j.aml.2025.109661.

Lin, S., Qiu, F., & Liu, D. (2010). Scattering of *SH*-waves by a scalene triangular hill. *Earthquake Engineering and Engineering Vibration*, 9, 23-38. 10.1007/s11803-009-8091-y.

Mojtabazadeh-Hasanlouei, S., Panji, M., & Kamalian, M. (2022a). Attenuated orthotropic time-domain half-space BEM for *SH*-wave scattering problems. *Geophysical Journal International*. 10.1093/gji/ggac032.

Mojtabazadeh-Hasanlouei, S., Panji, M., & Kamalian, M. (2022b). Scattering attenuation of transient *SH*-wave by an orthotropic Gaussian-shaped sedimentary basin. *Engineering Analysis with Boundary Elements*, 140, 186-219. 10.1016/j.enganabound.2022.04.023.

Mojtabazadeh-Hasanlouei, S., Panji, M. and Kamalian, M. (2024). A simple TD-BEM model for heterogeneous orthotropic hill-shaped topographies, *Discover Applied Sciences*, 6, 57. 10.1007/s42452-024-05695-7.

Parvanova, S. L., Dineva, P. S., Manolis, G. D., & Wuttke, F. (2014). Seismic response of lined tunnels in the half-plane with surface topography. *Bulletin of Earthquake Engineering*, 12(2), 981-1005. 10.1007/s10518-013-9546-0.

Schön, J. H. (2015). Physical properties of rocks: Fundamentals and principles of petrophysics (Chapter 4). *Developments in Petroleum Science*, 65, 109-118. 10.1016/B978-0-08-100404-3.00004-1.

Selivanov, M. (2019). An edge crack with cohesive zone in the orthotropic body. *Reports of the National Academy of Sciences of Ukraine*, (6), 25-34. 10.15407/dopovidi2019.06.025.

Tsaur, D., Chang, K., & Hsu, M. (2018). Ground motions around a deep semielliptic canyon with a horizontal edge subjected to incident plane *SH*-waves. *Journal of Seismology*, 22(6), 1579-1593. 10.1007/s10950-018-9787-0.

Teymouri, H., Khojasteh, A., Rahimian, M. & Pak, R. Y.S. (2021). An Analytical Solution of Wave Motion in a Transversely Isotropic Poroelastic Half-Space Underlying a Liquid Layer. *Civil Engineering Infrastructures Journal*, 54(1), 169-179. 10.22059/ceij.2020.283701.1592.

Zheng, T., & Dravinski, M. (1998). Amplification of *SH*-waves by an orthotropic basin. *Earthquake Engineering & Structural Dynamics*, 27, 243-257. 10.1002/(SICI)1096-9845(199803)27:3<243::AID-EQE727>3.0.CO;2-J.